Why Fe_3GaTe_2 has higher Curie temperature than Fe_3GeTe_2

Bomin Kim,[1] Tumentsereg Ochirkhuyag,[2] Dorj Odkhuu,[2,*] and S. H. Rhim[1,†]
[1]*Department of Physics, University of Ulsan, Ulsan 44610, Republic of Korea*
[2]*Department of Physics, Incheon National University, Incheon 22012, Republic of Korea*

(Received 20 January 2025; revised 17 April 2025; accepted 26 May 2026; published 24 June 2026)

Physics of Fe_3GaTe_2 having higher Curie temperature (T_C) than Fe_3GeTe_2 is explored theoretically in the framework of magnetic exchange interactions. Fe_3GaTe_2 and Fe_3GeTe_2 are isostructural, with Fe_3GaTe_2 having one less valence electron and smaller nearest-neighbor exchange coefficients (J_1 and J_2), challenging the conventional notion that larger J_1 or J_2 leads to a higher T_C. Based on the hybridization exchange, we show that higher-order exchange coefficients (J_3 or higher) are positive for Fe_3GaTe_2 but negative for Fe_3GeTe_2, due to a one-electron difference. As a consequence, total sum of all possible exchange coefficients in Fe_3GaTe_2 are larger than that for Fe_3GeTe_2, which accounts for higher T_C. To validate these findings, T_C values are computed using both mean-field theory and Monte Carlo simulation. Indeed, higher-order exchange interactions, when properly accounting for the number of neighbors, confirm the higher T_C of Fe_3GaTe_2.

DOI: 10.1103/g4v8-mrnd

I. INTRODUCTION

Two-dimensional van der Waals magnets offer unique opportunities for investigating fundamental magnetic models such as Ising, XY, and Heisenberg systems, providing a fertile ground for examining classic phenomena, including the Onsager solution [1], the Berezinskii-Kosterlitz-Thouless transition [2], and various forms of magnetic anisotropy [3,4].

Extensive research has been conducted [3–6] to achieve Curie temperatures (T_C) above room temperature. Among these, Fe_3GaTe_2 has attracted particular attention with T_C = 380 K surpassing room temperature [7–9]. Fe_3GaTe_2 is isostructural to Fe_3GeTe_2, replacing Ge by Ga with one less valence electron. The observation that the Curie temperature (T_C) of Fe_3GaTe_2 exceeds that of Fe_3GeTe_2 by over 100 K, despite differing by only one electron, warrants systematic investigation [10,11].

From previous study [4], Fe_3GaTe_2 and Fe_3GeTe_2 are presumably itinerant ferromagnets, whose spin Hamiltonian is conveniently expressed as sum of the Heisenberg exchange and the magnetic anisotropy, $H = -\sum_{i\neq j} J_{ij}\mathbf{S}_i \cdot \mathbf{S}_j - K_u \sum_i (\mathbf{S}_i \cdot \mathbf{e})^2$. J_{ij} is the magnetic exchange coefficient of two spins at atomic sites i and j; K_u is the magnetic anisotropy, where $\mathbf{e}$ is the unit vector along the magnetic easy axis. Noticeable T_C difference of two materials is intensively studied [12,13] in the framework of aforementioned spin Hamiltonian, more specifically in terms of magnetic exchange coefficients. It was suggested that larger nearest-neighbor exchange coefficient, J_1, of Fe_3GaTe_2 is responsible for higher T_C [14]. In another study, on the other hand, it was suggested that the magnetic exchange coefficients of third-nearest neighbor, J_3 and J_3', are the main factor of higher T_C of Fe_3GaTe_2 [15]. In this article, after examining both the magnetocrystalline anisotropy and the magnetic exchange coefficients, we show that higher-order magnetic exchange coefficients are indispensable for higher T_C of Fe_3GaTe_2. Moreover, the magnetic exchange coefficients with fully accounting number of neighbors are necessary in T_C estimation.

II. COMPUTATIONAL DETAILS

Figure 1 presents structure of Fe_3GaTe_2 and Fe_3GeTe_2 with different center atoms, Ga or Ge. Both Fe_3GaTe_2 and Fe_3GeTe_2 crystallize in a hexagonal structure with space group $P6_3/mmc$ (No. 194). The structure consists of one bilayer or two monolayer units, which are connected by the inversion symmetry. The monolayer unit contains quintuple sublayers. Two symmetrically distinct Fe atoms are distinguished as Fe(I) and Fe(II). The Fe(II)-Ga (or Ge) layer is sandwiched by Fe(I) and Te. Exchange interactions from J_1 to J_4 are shown in Fig. 1(b), where the intralayer interactions are identical in both layers. A detailed discussion will be provided later.

Density-functional calculations are carried out using the Vienna *ab initio* simulation package [16]. For Brillouin zone summation, $15 \times 15 \times 3$ k-mesh in Γ-centered scheme is used. Energy cutoff for plane-wave expansion is 500 eV. The generalized gradient approximation with Perdew, Burke, and Ernzerhof parametrization [17] is used for the exchange-correlation potential, where the interlayer van der Waals interactions are treated by the Grimme D3 dispersion correction (DFT-D3) method [18]. The atomic positions are optimized with the force criterion of 1 meV/Å. Additional self-consistent calculations are performed using the OPENMX package [19,20], which is based on the linear combination of pseudoatomic orbitals. The atomic basis sets for Fe, Ga, Ge, and Te are

*Contact author: odkhuu@inu.ac.kr
†Contact author: sonny@ulsan.ac.kr

Published by the American Physical Society under the terms of the Creative Commons Attribution 4.0 International license. Further distribution of this work must maintain attribution to the author(s) and the published article's title, journal citation, and DOI.

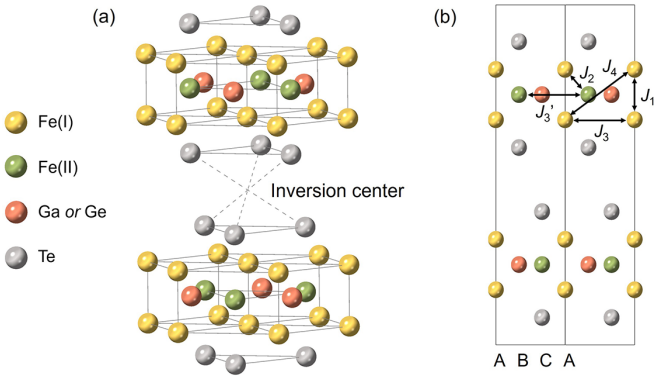


FIG. 1. (a) Crystal structure of Fe_3GaTe_2 and Fe_3GeTe_2. (b) The exchange parameters (from J_1 to J_4) are denoted in the structure. J_1, J_3, and J_4 indicate the interaction of Fe(I)-Fe(I); J_2 and J_3' for Fe(I)-Fe(II) and Fe(II)-Fe(II), respectively.

H-$s^3p^2d^2f^1$, $s^2p^2d^2$, $s^2p^2d^1$, and $s^2p^2d^2f^1$, respectively, with energy cutoff of 300 Ry and cutoff radii of 6.0 a.u. (Fe) and 7.0 a.u. (Ga, Ge, and Te). In the framework of the magnetic force theorem [21], the exchange coefficients are calculated using the Heisenberg model through implementation of the JX package [22–24]. From the exchange coefficients, T_C values are obtained using Monte Carlo simulation in the VAMPIRE package [25–28]. Atomistic spin Monte Carlo simulations are performed on a $4 \times 4 \times 16$ nm^3 cell (256 000 atoms) under periodic boundary conditions. Each temperature step involves 10 000 steps for equilibration, followed by 10 000 steps for thermal averaging. Magnetic moments for Fe_3GaTe_2 (Fe_3GeTe_2) are set to $\mu_{Fe(I)} = 2.46\,\mu_B$ ($2.61\mu_B$) and $\mu_{Fe(II)} = 1.48\,\mu_B$ ($1.58\mu_B$).

Magnetocrystalline anisotropy

Magnetocrystalline anisotropy (MCA) energy E_{MCA} is calculated from the total energy difference, $E_{MCA} = E(\parallel) - E(\perp)$, where $\parallel$ and $\perp$ indicate in-plane and perpendicular magnetizations, respectively, with spin-orbit coupling (SOC) included. Figure 2(a) shows total E_{MCA} for Fe_3GaTe_2 and Fe_3GeTe_2 in red and blue bars, respectively. $E_{MCA} = 1.38$ meV/f.u. of Fe_3GaTe_2 is smaller than $E_{MCA} = 3.15$ meV/f.u. of Fe_3GeTe_2, which agrees well with previous studies

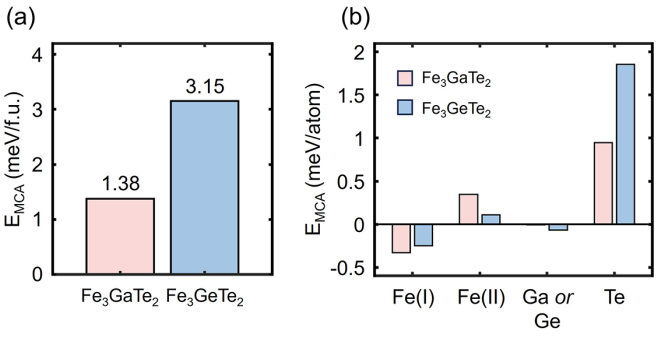


FIG. 2. (a) Total E_{MCA} (in meV/f.u.) of Fe_3GaTe_2 (1.38) and Fe_3GeTe_2 (3.15). (b) Atomic decomposition of E_{MCA} (in meV/atom) into Fe(I), Fe(II), Ga/Ge, and Te. Red and blue denote Fe_3GaTe_2 and Fe_3GeTe_2, respectively.

[10,29–32]. As presented in Fig. 2(b) for atomic-decomposed MCA, in both Fe_3GaTe_2 and Fe_3GeTe_2, contributions from two Fe sites exhibit different signs: Fe(I) contributes negatively, whereas Fe(II) contributes positively, while $|E_{MCA}[\text{Fe(I)}]|$ and $|E_{MCA}[\text{Fe(II)}]|$ are larger in Fe_3GaTe_2.

For MCA analysis, we focus on Fe sites although contributions of Te are much larger. Te contributions, from band analysis, are due to occupation change of p_x and p_y, which are strongly hybridized with Fe d orbitals. Hence, without loss of generality, Fe d-orbital-based analysis is sufficient. We provide Te p-orbital-based analysis in Appendix A. Figure 3 shows band structures of Fe(I) and Fe(II), where d orbitals are decomposed into the irreducible representations [33,34] d_{z^2}, $d_{xz/yz}$, and $d_{x^2-y^2/xy}$ or $m = 0, \pm1$, and ±2 in terms of magnetic quantum number m, respectively. In Fig. 3, red (blue) box denotes Fe_3GaTe_2 (Fe_3GeTe_2); left and right panels of each box are for Fe(I) and Fe(II), respectively. Upper (lower) panels are for the majority (minority) spin channel, denoted hereafter as $\uparrow$ ($\downarrow$). In rigid-band picture, Fe_3GaTe_2 bands are downward shift of E_F of Fe_3GeTe_2 bands due to one less valence electron.

In MCA analysis, the framework of the second-order perturbation theory is employed [32,35–38],

$$E_{MCA} = \xi^2 \sum_{\sigma,\sigma',o,u} \frac{|\langle o,\sigma|L_z|u,\sigma'\rangle|^2 - |\langle o,\sigma|L_x|u,\sigma'\rangle|^2}{E_{u,\sigma} - E_{o,\sigma'}}. \tag{1}$$

ξ is the strength of spin-orbit coupling; o (u) stands for the occupied (unoccupied) state; σ and σ' denote spin states; and L_z (L_x) is the orbital angular momentum operator for the z (x) component. In the following, MCA analysis is presented based on d manifold of Fe(I) and Fe(II) by comparing Fe_3GaTe_2 and Fe_3GeTe_2 band structures. Fe_3GaTe_2 is discussed first and then relative change in Fe_3GeTe_2 follows.

For Fe(I) in Fe_3GaTe_2, $E_{MCA} < 0$ arises through the spin-flip channel, $\langle d_{xz/yz}, \uparrow (\downarrow)|L_z|d_{xz/yz}, \downarrow (\uparrow)\rangle$, where bra (ket) denotes occupied (unoccupied) state. Spin states with parentheses, $\uparrow$ ($\downarrow$) and $\downarrow$ ($\uparrow$), indicate states in both $\uparrow$ and $\downarrow$ states. As mentioned earlier, in a simplistic picture, Fe_3GaTe_2 bands are downward shift of E_F of Fe_3GeTe_2 bands. For Fe_3GeTe_2, as $d_{xz/yz}$ bands become occupied near KM and at H in the $\uparrow$ channel, $E_{MCA} > 0$ contributions from $\langle d_{xz/yz}, \uparrow |L_z|d_{xz/yz}, \uparrow\rangle$ increase. As a consequence, $|E_{MCA}[\text{Fe(I)}]|$ reduces in Fe_3GeTe_2.

For Fe(II) in Fe_3GaTe_2, $E_{MCA} > 0$ comes from the same spin channel, $\langle d_{xz/yz}, \uparrow (\downarrow)|L_z|d_{xz/yz}, \uparrow (\downarrow)\rangle$, except near K and H. Other $E_{MCA} > 0$, near K and H, arises from $\langle d_{x^2-y^2/xy}, \downarrow |L_z|d_{x^2-y^2/xy}, \downarrow\rangle$. In Fe_3GeTe_2, $d_{xz/yz}$ in the $\uparrow$ channel are occupied near KM and H, giving $E_{MCA} < 0$ by $\langle d_{xz/yz}, \uparrow |L_z|d_{xz/yz}, \downarrow\rangle$ in the spin-flip channel. Moreover, occupied $d_{x^2-y^2/xy}$ in the $\uparrow$ channel near K leads to $E_{MCA} < 0$ through the spin-flip channel $\langle d_{x^2-y^2/xy}, \uparrow |L_z|d_{x^2-y^2/xy}, \downarrow\rangle$. As a result, in Fe_3GeTe_2, $|E_{MCA}[\text{Fe(II)}]|$ reduces.

So far, the E_{MCA} difference between Fe_3GaTe_2 and Fe_3GeTe_2 has been investigated through Fe band analysis. Total E_{MCA} values of Fe_3GaTe_2 and Fe_3GeTe_2 are 1.38 and 3.15 meV/f.u., respectively. Among the two terms of the Hamiltonian mentioned earlier, the energy scale of MCA is

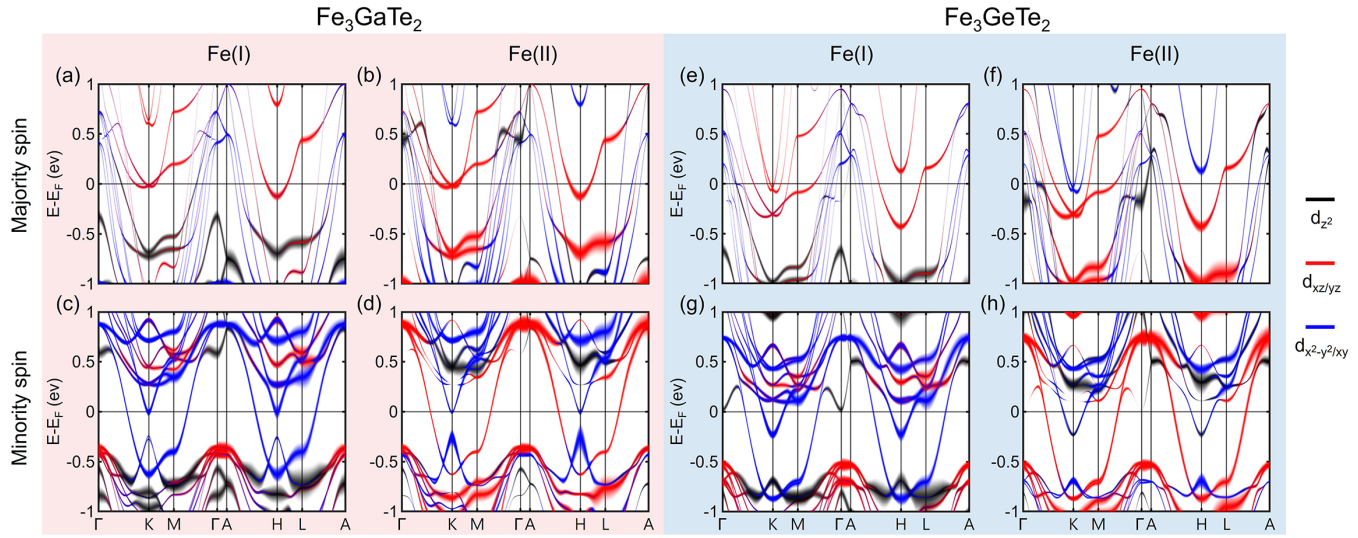


FIG. 3. Band structures in d-orbital projection. (a)–(d) Fe_3GaTe_2 in red box and (e)–(h) Fe_3GeTe_2 in blue box. In each box, left and right panels for Fe(I) and Fe(II), respectively. Upper (lower) panels for the majority (minority) spin channel. d-orbital decomposition into d_{z^2} (black line), $d_{xz/yz}$ (red line), and $d_{x^2-y^2/xy}$ (blue line) according to the irreducible representation of hexagonal symmetry.

smaller than that of J. It is insufficient to discuss T_C with MCA alone. Hence, the magnetic exchange coefficients are discussed by comparing Fe_3GaTe_2 and Fe_3GeTe_2.

III. MAGNETIC EXCHANGE COEFFICIENTS AND CURIE TEMPERATURE

A schematic of the magnetic exchange interactions is shown in Fig. 1(b), where pair distance increases from J_1 to J_4. J_1 represents the exchange interaction between vertical Fe(I) pairs, while J_3 and J_3' correspond to horizontal interactions between Fe(I)-Fe(I) and Fe(II)-Fe(II), respectively. J_2 and J_4 indicate diagonal interactions of Fe(I)-Fe(II) and Fe(I)-Fe(I), respectively. Calculated J_{ij} values under the distances in Fe_3GaTe_2 and Fe_3GeTe_2 are shown in Figs. 5(a) and 5 (b), respectively. In our convention, positive (negative) value of J reflects parallel (antiparallel) spin arrangement.

The nearest and second-nearest neighbors, J_1 and J_2, are 48.67 meV (78.84 meV) and 18.54 meV (24.61 meV) for Fe_3GaTe_2 (Fe_3GeTe_2), respectively. As other studies have reported [7,15,29], J_1 and J_2 of Fe_3GaTe_2 are smaller than those of Fe_3GeTe_2. In conventional wisdom, larger J_1 and J_2 imply higher T_C. However, this is not observed in our case as T_C of Fe_3GaTe_2 is more than that of 100 K higher than that of Fe_3GeTe_2.

In the mean-field approximation [39,40], T_C for one magnetic sublattice is $T_C \approx \frac{1}{k_B} z J_1$, where z is the number of neighbors and k_B is the Boltzmann constant. In this case, only one magnetic exchange coefficient, J_1, is necessary. On the other hand, when the number of sublattices is more than one, it

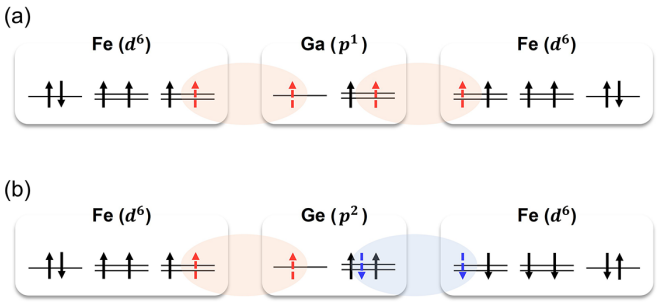


FIG. 4. Schematics of the hybridization exchange between Fe atoms for (a) Fe_3GaTe_2 and (b) Fe_3GeTe_2. Fe exchange interaction is mediated by hybridization with Ga or Ge. Red and blue circles indicate the hybridization. Nominal valencies of Fe, Ga, and Ge are d^6, p^1, and p^2, respectively.

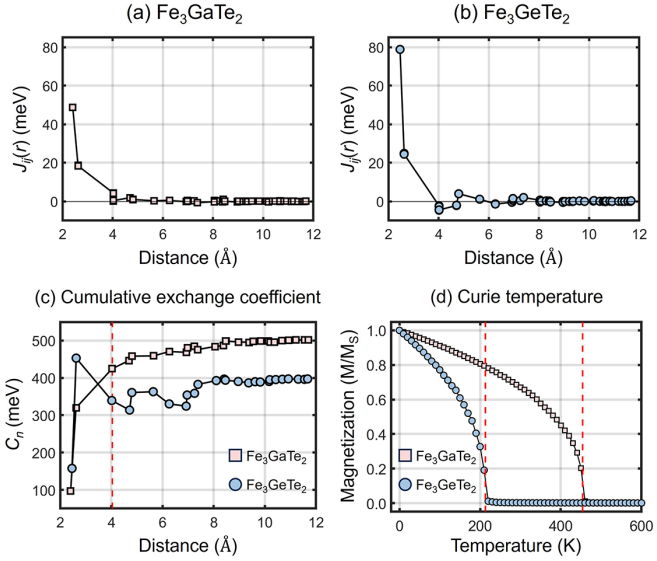


FIG. 5. The exchange interaction coefficients as a function of distance for (a) Fe_3GaTe_2 and (b) Fe_3GeTe_2. (c) The cumulative all J_n, $C_n = \sum_i^n z_i J_i$, with respect to the atomic distance. (d) The normalized magnetization as a function of temperature. Fe_3GaTe_2 and Fe_3GeTe_2 show T_C values of 456 and 213 K, respectively. Red and blue spheres denote Fe_3GaTe_2 and Fe_3GeTe_2, respectively.

TABLE I. Magnetic exchange coefficients (J_n), effective exchange coefficients (z_nJ_n), and relevant atomic distances (d_n) of Fe_3GaTe_2 and Fe_3GeTe_2. J_1 to J_4 (in meV) as sketched in Fig. 1; J_n and z_nJ_n in meV, where z_n is the number of neighbors; d_n is given in Å.

		J_1	J_2	J_3	J_3'	J_4
	Type	Fe(I)-Fe(I)	Fe(I)-Fe(II)	Fe(I)-Fe(I)	Fe(II)-Fe(II)	Fe(I)-Fe(I)
	z_n	1	6	12	6	6
Fe_3GaTe_2	J_n	48.67	18.54	4.23	0.26	1.85
	z_nJ_n	48.67	111.24	50.76	1.56	11.10
	d_n	2.41	2.62	4.03	4.03	4.70
Fe_3GeTe_2	J_n	78.84	24.61	−2.46	−4.56	−2.13
	z_nJ_n	78.84	147.66	−29.52	−27.36	−12.78
	d_n	2.46	2.63	4.02	4.02	4.71

is not so simple. For an Ising magnet containing two magnetic sublattices A and B, T_C is obtained from eigenvalues of the 2×2 interaction matrix [40–43],

$$T_C = \frac{1}{2k_B}(z_1J_{AA} + z_2J_{BB}) + \frac{1}{2k_B}\sqrt{(z_1J_{AA} - z_2J_{BB})^2 + 4(z_3J_{AB})^2}, \quad (2)$$

where J_{AA} and J_{BB} are the intrasublattice exchange constants and J_{AB} represents the intersublattice interactions. Clearly, instead of single J_1, three magnetic exchange coefficients are necessary. For the system with three magnetic sublattices, it is necessary to diagonalize the 3×3 matrix. Extension of Eq. (2) becomes more complicated, as six J terms are necessary and one needs to solve the cubic equation (see Appendix B). In Fe_3GaTe_2 or Fe_3GeTe_2, the number of sublattices is more than two. As discussed, higher-order J (i.e., J_3 and above) cannot be ignored.

Table I lists magnetic exchange coefficients, J_n (n = 1, 2, 3, 4), with distances between atoms (d_n). As J_n has more than one neighbor, we introduce the effective magnetic exchange coefficients, z_nJ_n, where z_n is the number of neighbors. Two remarkable features are apparent: (1) opposite signs of J_n ($n \geqslant 3$) for Fe_3GaTe_2 (positive) and Fe_3GeTe_2 (negative), and (2) much larger z_n for the higher-order J_n than that of J_1. To easily visualize higher-order contribution, we further introduce the cumulative exchange coefficient, $C_n = \Sigma_{i=1}^{n} z_iJ_i$, summation of the effective magnetic exchange coefficients. Figure 5(c) plots C_n as a function of d_n. When $d_n < 4$ Å ($n < 3$), C_n of Fe_3GaTe_2 is smaller than that of Fe_3GeTe_2. When $d_n \geqslant 4$ Å ($n \geqslant 3$), on the other hand, Fe_3GaTe_2 has larger C_n than Fe_3GeTe_2 because all $J > 0$ for Fe_3GaTe_2, while $J_n < 0$ ($n \geqslant 3$) for Fe_3GeTe_2. The physics of opposite signs of higher-order J_n ($n \geqslant 3$) is discussed in the next paragraph. Large z_n of higher-order J_n reflects the role of the hexagonal structure. For example, with $z_1 = 1$ and $z_2 = 6$, $z_1J_1 < z_2J_2$ even though $J_1 > J_2$. Moreover, z_3J_3 is larger than z_1J_1 in Fe_3GaTe_2. If both were simple cubic ($z_1 = 6$, $z_2 = 12$), C_n of Fe_3GaTe_2 would become smaller than that of Fe_3GeTe_2.

The opposite signs of higher-order J are analyzed schematically in Fig. 4 by the hybridization exchange. Fe-Fe exchange interaction is mediated by hybridization with Ga/Ge as the Fe-Ga/Ge distance is much shorter than the Fe-Fe one. Hybridization at both sides (metal-ligand and ligand-metal) occurs simultaneously, where the occupancy of ligand determines the sign of the exchange. The hybridization exchange differs from superexchange, where hopping from metal to ligand and then from ligand to metal takes place sequentially. Furthermore, the hybridization exchange is nonperturbative, well accounting the long-range interaction in metallic magnet.

More specifically, in Fig. 4, nominal valency of Fe is d^6 in good approximation; those of Ga and Ge are p^1 and p^2, respectively. For Fe_3GaTe_2, the parallel spin configuration enables J_3, $J_3' > 0$ by Fe-Ga p-d hybridization. On the other hand, for Fe_3GaTe_2, the Pauli exclusion principle prevents the parallel spin configuration owing to p^2 occupation; hence J_3, $J_3' < 0$. Further orbital-resolved J_3 and partial density of states analyses are provided in Appendix C. Based on the hybridization exchange, it is expected that any ligand element with p^0 or p^1 leads to high T_C owing to $J > 0$ (see Appendix D).

From Monte Carlo simulations using VAMPIRE software package [25–28], the reduced magnetizations as a function of temperature are calculated for Fe_3GaTe_2 and Fe_3GeTe_2, as plotted in Fig. 5(d) with magnetic exchange coefficients up to 25th order, including the interlayer interactions. By fitting to $m(T) = (1 - T/T_C)^{\beta}$ [26,44], the critical exponent β and the T_C were determined, where $m = M/M_s$ is the reduced magnetization for the saturation magnetization M_s. From Fig. 5(d), T_C values are determined to be 456.5 and 213.8 K for Fe_3GaTe_2 and Fe_3GeTe_2. Our determined T_C is higher (lower) than the experimental ones in Fe_3GaTe_2 (Fe_3GeTe_2). Alternatively, T_C is determined from the eigenvalue equation in the mean-field approximation for three magnetic sublattices, including higher order up to J_6 (see Appendix B). By this, T_C values are 307.6 and 219.7 K for Fe_3GaTe_2 and Fe_3GeTe_2, respectively, which are lower than the experimental ones [10,11]. The critical exponents, extracted from Fig. 5, are β = 0.38 and 0.41 for Fe_3GaTe_2 and Fe_3GeTe_2, respectively, slightly larger than $\beta = 0.325$ from the three-dimensional Ising model [45]. Furthermore, the scaling behaviors of the magnetic exchange coefficients, $J(r) \approx 1/r^{\delta}$, with respect to distance are δ=4.93 and 4.79 for Fe_3GaTe_2 and Fe_3GeTe_2, respectively, slightly larger than $\delta = 4.5$ of the mean-field approximation and 4.6 of the previous study for Fe_3GeTe_2 [45].

IV. SUMMARY

In summary, Fe_3GaTe_2's higher T_C is investigated. Fe_3GaTe_2 has smaller E_{MCA} (1.38 meV/f.u.) than Fe_3GeTe_2

(3.15 meV/f.u.). The difference of MCA is analyzed from band structure perspective, where E_F shift associated with one-electron difference is responsible. As contribution of the magnetic exchange is more dominant in spin Hamiltonian, magnetic exchange coefficients are exhaustively investigated up to sixth order or higher. While Fe_3GaTe_2 has smaller magnetic exchange coefficients for the nearest and second-nearest neighbors, J_1 and J_2, the cumulative exchange coefficients ($C_n = \sum_i^n z_i J_i$), with fully accounting number of neighbors, are larger, which supports higher T_C of Fe_3GaTe_2. The opposite signs of higher-order J's in two materials are interpreted by hybridization exchange, where the orbital hybridization determines the sign of long-range J. Furthermore, T_C values are determined as 456.5 and 213.8 K for Fe_3GaTe_2 and Fe_3GeTe_2, respectively, using Monte Carlo simulation. Alternatively, T_C values from the eigenvalue equation in the mean-field approximation are 307.6 and 219.7 K, respectively.

ACKNOWLEDGMENTS

This research was supported by National Research Foundation of Korea (Grants No. RS-2024-00407298, No. RS-2022-NR068225, No. 287 RS-2024-00451261, and No. RS-2024-00449996) and National Research Council of Science & Technology (NST) Grant No. CAP25061-000. We are also grateful for support by the National Supercomputing Center from supercomputing resources (Grant No. KSC-2025-CRE-0016).

DATA AVAILABILITY

The data that support the findings of this article are not publicly available. The data are available from the authors upon reasonable request.

APPENDIX A: Te BAND ANALYSIS FOR E_{MCA}

Te exhibits a larger E_{MCA} in Fe_3GeTe_2 compared to Fe_3GaTe_2. Figure 6 shows the Te band structures, where the p orbitals are decomposed into the irreducible representations of p_z (black lines) and $p_{x/y}$ (red lines). In Fig. 6, the red and blue boxes denote Fe_3GaTe_2 and Fe_3GeTe_2, respectively, while the upper and lower panels correspond to the majority and minority spin channels. In both structures, $E_{\mathrm{MCA}} > 0$ mainly comes from $\langle p_{x/y}, \uparrow | L_z | p_{x/y}, \uparrow \rangle$. In the majority spin channel of Fe_3GaTe_2, bands with relatively higher $p_{x/y}$ weights are in the unoccupied state, whereas those with lower weights are occupied. In Fe_3GeTe_2, bands with higher $p_{x/y}$ weights become occupied near $M\Gamma$. Therefore, although the same matrix $\langle p_{x/y}, \uparrow | L_z | p_{x/y}, \uparrow \rangle$ induces $E_{\mathrm{MCA}} > 0$ in both structures, Fe_3GeTe_2 has a larger value due to the higher orbital weight of the bands in the occupied state.

APPENDIX B: MEAN-FIELD MODEL FOR THREE-MAGNETIC-SUBLATTICES SYSTEM

In the mean-field approximation, T_C for a one-magnetic-sublattice system is expressed as

$$T_C \approx \frac{1}{k_B} z J_1, \tag{B1}$$

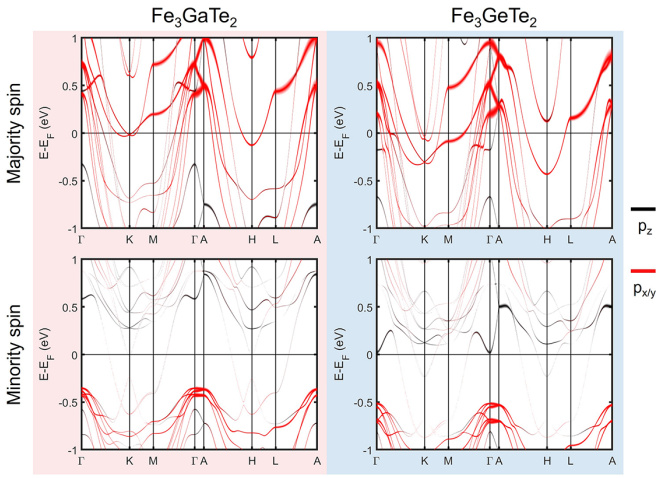


FIG. 6. Band structures of Te in p-orbital projection. Fe_3GaTe_2 and Fe_3GeTe_2 in red box and blue box, respectively. Upper (lower) panels for the majority (minority) spin channel. p-orbital decomposition into p_z (black line) and $p_{x/y}$ (red line) according to the irreducible representation of hexagonal symmetry.

where k_B is the Boltzmann constant, z is the number of nearest neighbors, and J_1 is the nearest-neighbor exchange coefficient. For an Ising magnet with two magnetic sublattices A and B, the secular equation of the Hamiltonian gives the eigenvalue equation [40]

$$\begin{vmatrix} x - J_{AA} & -J_{AB} \\ -J_{AB} & x - J_{BB} \end{vmatrix} = 0, \tag{B2}$$

where $x = k_B T$; J_{AA} and J_{BB} denote the intrasublattice exchange coefficients for sublattices A and B, respectively; and J_{AB} represents the intersublattice interaction. For simplicity, the number of interactions is set to unity ($z = 1$) without loss of generality. Solving Eq. (B2) yields

$$T_C = \frac{1}{2k_B}(J_{AA} + J_{BB}) + \frac{1}{2k_B}\sqrt{(J_{AA} - J_{BB})^2 + 4J_{AB}^2}. \tag{B3}$$

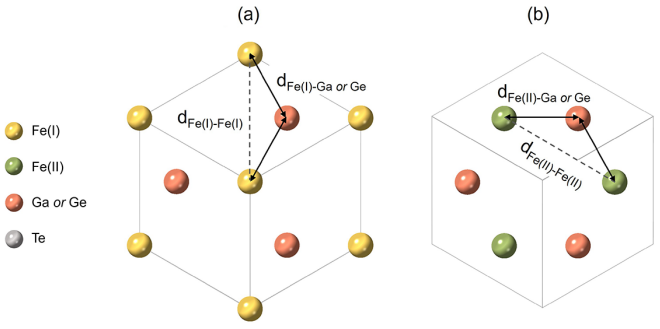
As clearly demonstrated, to obtain T_C not only one J but two additional J terms are required. For a system with three magnetic sublattices (A, B, and C), the 3×3 secular equation is

$$\begin{vmatrix} x - J_{AA} & -J_{AB} & -J_{CA} \\ -J_{AB} & x - J_{BB} & -J_{BC} \\ -J_{CA} & -J_{BC} & x - J_{CC} \end{vmatrix} = 0, \tag{B4}$$

where J_{AA}, J_{BB}, and J_{CC} are the intrasublattice exchange coefficients for sublattices A, B, and C, respectively; J_{AB}, J_{BC}, and J_{CA} are the intersublattice interactions. Equation (B4) is a cubic equation for x,

$$\begin{aligned} & x^3 - (J_{AA} + J_{BB} + J_{CC})x^2 \\ & - (J_{AB}^2 + J_{BC}^2 + J_{CA}^2 - J_{AA}J_{BB} - J_{CC}J_{AA} - J_{BB}J_{CC})x \\ & - J_{AA}J_{BB}J_{CC} - 2J_{AB}J_{BC}J_{CA} \\ & + J_{AA}J_{BC}^2 + J_{BB}J_{CA}^2 + J_{CC}J_{AB}^2 = 0, \end{aligned} \tag{B5}$$

which needs six J terms. In general, it can be solved using Cardano's formula. For Fe_3GaTe_2, we obtain 307.63, 307.63, and 1.31×10^{-18}; for Fe_3GeTe_2, 219.66, 3.82×10^{9}, and



(c)

	J_3		J_3'	
	$d_{Fe(I)-Fe(I)}$	$d_{Fe(I)-Ga\ or\ Ge}$	$d_{Fe(II)-Fe(II)}$	$d_{Fe(II)-Ga\ or\ Ge}$
Fe_3GaTe_2	4.03 Å	2.62 Å	4.03 Å	2.33 Å
Fe_3GeTe_2	4.02 Å	2.63 Å	4.02 Å	2.32 Å

FIG. 7. The top view of the structures for (a) J_3 and (b) J_3' shows only the atoms involved in each exchange interaction for better visibility. The distances between atoms are shown in panel (c); the Fe-Ga/Ge distances are shorter than the Fe-Fe distances.

3.82×10^9. T_C values of 307.63 and 219.66 K are in close agreement with the experimental results, 380 and 230 K, for Fe_3GaTe_2 and Fe_3GeTe_2, respectively.

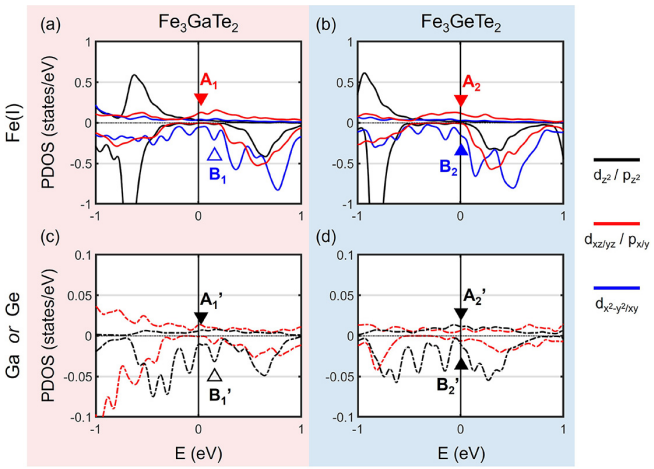
APPENDIX C: THE HYBRIDIZATION EXCHANGE

The opposite signs of higher-order J in Fe_3GaTe_2 and Fe_3GeTe_2 are analyzed. More specifically, we focus on the opposite signs of J_3 and J_3' based on the hybridization exchange model. The hybridization of Fe-Ga/Ge is justified by partial density of states (PDOS) analysis.

For J_3 and J_3', Fe atoms are far away, distance exceeding 4 Å. Figure 7 shows atoms relevant for J_3 and J_3' for better visibility, where atom-atom distances are listed in Fig. 7(c). Clearly, Fe-Ga/Ge distances are much shorter than Fe-Fe ones. Hence, the exchange interactions between Fe-Fe sites, characterized by J_3 and J_3', are indirect exchange interactions mediated by Ga/Ge atoms via Fe-Ga/Ge hybridization.

As mentioned in the main text, the sign of this hybridization exchange is determined by the electron occupancy of the Ga/Ge p orbitals. To confirm, PDOS analysis is performed for orbital-resolved J_3. Figures 8(a)–8(d) present PDOS, where left and right panels are for Fe_3GaTe_2 and Fe_3GeTe_2, respectively, while upper and lower panels show Fe(I) and Ga/Ge, respectively. d and p orbitals are denoted by solid and dashed lines, respectively; important peaks are labeled by A_1, A_2, B_1, B_2, and their variants. In the majority spin state, A_1 and A_1' of Fe(I) $d_{xz/yz}$ and Ga p_z in Fe_3GaTe_2 are hybridized and partially occupied. Similarly, in Fe_3GeTe_2, A_2 and A_2' of Fe(I) $d_{xz/yz}$ and Ge p_z are also hybridized and partially occupied. In the minority spin state, B_1 and B_1' of Fe(I) $d_{x^2-y^2/xy}$ and Ga p_z in Fe_3GaTe_2 are hybridized and unoccupied. On the other hand, in Fe_3GeTe_2, B_2 and B_2' of Fe(I) $d_{x^2-y^2/xy}$ and Ge p_z are hybridized and partially occupied.

Figures 8(e) and 8(f) show the orbital-resolved J_3 in Fe_3GaTe_2 and Fe_3GeTe_2, respectively. Fe_3GaTe_2 exhibits a large $J > 0$ from $d_{xz/yz}$–$d_{xz/yz}$ interactions, while Fe_3GeTe_2 shows a large $J < 0$ from $d_{x^2-y^2/xy}$–$d_{x^2-y^2/xy}$ interactions. Due to different occupation as well as hybridization with Ga/Ge, as



(e) J_3 in Fe_3GaTe_2

[meV]	d_{z^2}	$d_{xz/yz}$	$d_{x^2-y^2/xy}$
d_{z^2}	−0.05	−0.64	0.16
$d_{xz/yz}$	−0.64	6.08	−0.52
$d_{x^2-y^2/xy}$	0.16	−0.52	−0.56

(f) J_3 in Fe_3GeTe_2

[meV]	d_{z^2}	$d_{xz/yz}$	$d_{x^2-y^2/xy}$
d_{z^2}	−0.09	−0.60	0.01
$d_{xz/yz}$	−0.60	0.62	−0.10
$d_{x^2-y^2/xy}$	0.01	−0.10	−2.41

FIG. 8. Partial density of states of Fe(I) in (a) Fe_3GaTe_2 and (b) Fe_3GeTe_2, and of Fe(II) in (c) Fe_3GaTe_2 and (d) Fe_3GeTe_2. Orbital-resolved J_3 in (e) Fe_3GaTe_2 and (f) Fe_3GeTe_2. Fe_3GaTe_2 exhibits a large positive J value from $d_{xz/yz}$-$d_{xz/yz}$ interactions, while Fe_3GeTe_2 shows a large negative J value from $d_{x^2-y^2/xy}$-$d_{x^2-y^2/xy}$ interactions.

described above, J_3 values in Fe_3GaTe_2 and Fe_3GeTe_2 exhibit different signs and orbital contributions.

APPENDIX D: THE PREDICTIVE CAPABILITY OF THE HYBRIDIZATION EXCHANGE

The hybridization exchange can be applied for discovery or exploration of higher-T_C materials, at least for metallic ferromagnets with the same class as Fe_3GeTe_2. As an example, we provide our preliminary study of Fe_3AlTe_2 and Fe_3SiTe_2, which have the same crystal structure and the valence electrons as Fe_3GaTe_2 and Fe_3GeTe_2, respectively. Due to the

	J_N	J_1	J_2	J_3	J_3'	J_4	
	Type	Fe(I)-Fe(I)	Fe(I)-Fe(II)	Fe(I)-Fe(I)	Fe(II)-Fe(II)	Fe(I)-Fe(I)	
	N	1	6	12	6	6	
Fe_3GaTe_2	Distance (Å)	2.41	2.62	4.03	4.03	4.70	
	J_{ij} (meV)	48.67	18.54	4.23	0.26	1.85	p^1
Fe_3AlTe_2	Distance (Å)	2.40	2.62	4.03	4.03	4.69	
	J_{ij} (meV)	45.10	19.16	5.35	0.84	1.54	
Fe_3GeTe_2	Distance (Å)	2.46	2.63	4.02	4.02	4.71	
	J_{ij} (meV)	78.84	24.61	−2.46	−4.56	−2.13	p^2
Fe_3SiTe_2	Distance (Å)	2.42	2.57	3.93	3.93	4.62	
	J_{ij} (meV)	87.19	24.13	−5.35	−2.98	−4.13	

FIG. 9. Exchange interaction coefficients from J_1 to J_4 of Fe_3GaTe_2, Fe_3AlTe_2, Fe_3GeTe_2, and Fe_3SiTe_2. Fe_3GaTe_2 and Fe_3AlTe_2 show positive values from J_1 to J_4, while Fe_3GeTe_2 and Fe_3SiTe_2 show negative values from J_3 to J_4.

identical crystal structure, the crystal field split electronic configurations of Fe_3AlTe_2 and Fe_3SiTe_2 are the same as those of Fe_3GaTe_2 and Fe_3GeTe_2.

Figure 9 shows J values: J_3 or higher are positive for Fe_3AlTe_2 as Fe_3GaTe_2; J_3 or higher are negative for Fe_3SiTe_2 as Fe_3GeTe_2. In other words, the p^1 configuration of Ga and Al enables ferromagnetic coupling ($J > 0$), whereas the p^2 configuration of Ge and Si prevents ferromagnetic coupling ($J < 0$). Based on the positive higher-order J, a higher T_C is expected for Fe_3AlTe_2 compared to Fe_3SiTe_2.

[1] L. Onsager, Crystal statistics. I. A two-dimensional model with an order-disorder transition, Phys. Rev. **65**, 117 (1944).

[2] J. M. Kosterlitz and D. J. Thouless, Ordering, metastability and phase transitions in two-dimensional systems, J. Phys. C **6**, 1181 (1973).

[3] M. Gibertini, M. Koperski, A. F. Morpurgo, and K. S. Novoselov, Magnetic 2D materials and heterostructures, Nat. Nanotechnol. **14**, 408 (2019).

[4] K. S. Burch, D. Mandrus, and J.-G. Park, Magnetism in two-dimensional van der Waals materials, Nature (London) **563**, 47 (2018).

[5] B. Huang, G. Clark, E. Navarro-Moratalla, D. R. Klein, R. Cheng, K. L. Seyler, D. Zhong, E. Schmidgall, M. A. McGuire, D. H. Cobden, *et al.*, Layer-dependent ferromagnetism in a van der Waals crystal down to the monolayer limit, Nature (London) **546**, 270 (2017).

[6] C. Gong, L. Li, Z. Li, H. Ji, A. Stern, Y. Xia, T. Cao, W. Bao, C. Wang, Y. Wang, *et al.*, Discovery of intrinsic ferromagnetism in two-dimensional van der Waals crystals, Nature (London) **546**, 265 (2017).

[7] D. Li, S. Haldar, T. Drevelow, and S. Heinze, Tuning the magnetic interactions in van der Waals Fe_3GeTe_2 heterostructures: A comparative study of *ab initio* methods, Phys. Rev. B **107**, 104428 (2023).

[8] W. Jin, G. Zhang, H. Wu, L. Yang, W. Zhang, and H. Chang, Room-temperature and tunable tunneling magnetoresistance in Fe_3GaTe_2-based 2D van der Waals heterojunctions, ACS Appl. Mater. Interfaces **15**, 36519 (2023).

[9] C. Wang, J. Wang, W.-Q. Xie, G. Zhang, H. Wu, J. Zhou, X. Zhu, W. Ning, G. Wang, C. Tan, *et al.*, Sign-tunable exchange bias effect in proton-intercalated Fe_3GaTe_2 nanoflakes, Phys. Rev. B **107**, L140409 (2023).

[10] G. Zhang, F. Guo, H. Wu, X. Wen, L. Yang, W. Jin, W. Zhang, and H. Chang, Above-room-temperature strong intrinsic ferromagnetism in 2D van der Waals Fe_3GaTe_2 with large perpendicular magnetic anisotropy, Nat. Commun. **13**, 5067 (2022).

[11] H.-J. Deiseroth, K. Aleksandrov, C. Reiner, L. Kienle, and R. K. Kremer, Fe_3GeTe_2 and Ni_3GeTe_2-two new layered transition-metal compounds: Crystal structures, HRTEM investigations, and magnetic and electrical properties, Eur. J. Inorg. Chem. **2006**, 1561 (2006).

[12] B. Marfoua and J. Hong, Large anomalous transverse transport properties in atomically thin 2D Fe_3GaTe_2, NPG Asia Mater. **16**, 6 (2024).

[13] H. Wu, C. Hu, Y. Xie, B. G. Jang, J. Huang, Y. Guo, S. Wu, C. Hu, Z. Yue, Y. Shi, *et al.*, Spectral evidence for local-moment ferromagnetism in the van der Waals metals Fe_3GaTe_2 and Fe_3GeTe_2, Phys. Rev. B **109**, 104410 (2024).

[14] J.-E. Lee, S. Yan, S. Oh, J. Hwang, J. D. Denlinger, C. Hwang, H. Lei, S.-K. Mo, S. Y. Park, and H. Ryu, Electronic structure of above-room-temperature van der Waals ferromagnet Fe_3GaTe_2, Nano Lett. **23**, 11526 (2023).

[15] A. M. Ruiz, D. L. Esteras, D. López-Alcalá, and J. J. Baldoví, On the origin of the above-room-temperature magnetism in the 2D van der Waals ferromagnet Fe_3GaTe_2, Nano Lett. **24**, 7886 (2024).

[16] G. Kresse and J. Furthmüller, Efficient iterative schemes for *ab initio* total-energy calculations using a plane-wave basis set, Phys. Rev. B **54**, 11169 (1996).

[17] J. P. Perdew, K. Burke, and M. Ernzerhof, Generalized gradient approximation made simple, Phys. Rev. Lett. **77**, 3865 (1996).

[18] S. Grimme, J. Antony, S. Ehrlich, and H. Krieg, A consistent and accurate *ab initio* parametrization of density functional dispersion correction (DFT-D) for the 94 elements H-Pu, J. Chem. Phys. **132**, 154104 (2010).

[19] T. Ozaki, Variationally optimized atomic orbitals for large-scale electronic structures, Phys. Rev. B **67**, 155108 (2003).

[20] T. Ozaki and H. Kino, Numerical atomic basis orbitals from H to Kr, Phys. Rev. B **69**, 195113 (2004).

[21] A. I. Liechtenstein, M. Katsnelson, V. Antropov, and V. Gubanov, Local spin density functional approach to the theory of exchange interactions in ferromagnetic metals and alloys, J. Magn. Magn. Mater. **67**, 65 (1987).

[22] H. Yoon, T. J. Kim, J.-H. Sim, S. W. Jang, T. Ozaki, and M. J. Han, Reliability and applicability of magnetic-force linear response theory: Numerical parameters, predictability, and orbital resolution, Phys. Rev. B **97**, 125132 (2018).

[23] H. Yoon, T. J. Kim, J.-H. Sim, and M. J. Han, Jx: An open-source software for calculating magnetic interactions based on magnetic force theory, Comput. Phys. Commun. **247**, 106927 (2020).

[24] https://kaist-elst.github.io/Jx.jl/.

[25] N. Metropolis, A. W. Rosenbluth, M. N. Rosenbluth, A. H. Teller, and E. Teller, Equation of state calculations by fast computing machines, J. Chem. Phys. **21**, 1087 (1953).

[26] R. F. L. Evans, W. J. Fan, P. Chureemart, T. A. Ostler, M. O. A. Ellis, and R. W. Chantrell, Atomistic spin model simulations of magnetic nanomaterials, J. Phys.: Condens. Matter **26**, 103202 (2014).

[27] P. Asselin, R. F. L. Evans, J. Barker, R. W. Chantrell, R. Yanes, O. Chubykalo-Fesenko, D. Hinzke, and U. Nowak, Constrained Monte Carlo method and calculation of the temperature dependence of magnetic anisotropy, Phys. Rev. B **82**, 054415 (2010).

[28] https://vampire.york.ac.uk/.

[29] X. Li, M. Zhu, Y. Wang, F. Zheng, J. Dong, Y. Zhou, L. You, and J. Zhang, Tremendous tunneling magnetoresistance effects based on van der Waals room-temperature ferromagnet Fe_3GaTe_2 with highly spin-polarized Fermi surfaces, Appl. Phys. Lett. **122**, 082404 (2023).

[30] H. L. Zhuang, P. R. C. Kent, and R. G. Hennig, Strong anisotropy and magnetostriction in the two-dimensional Stoner ferromagnet Fe_3GeTe_2, Phys. Rev. B **93**, 134407 (2016).

[31] Y.-P. Wang, X.-Y. Chen, and M.-Q. Long, Modifications of magnetic anisotropy of Fe_3GeTe_2 by the electric field effect, Appl. Phys. Lett. **116**, 092404 (2020).

[32] B. Kim, Q. ul ain, and S. H. Rhim, Strain tunability of magnetocrystalline anisotropy in Fe_3GeTe_2 thin films, Phys. Rev. B **109**, 174434 (2024).

[33] J. Sakurai and J. Napolitano, *Modern Quantum Mechanics* (Pearson, Boston, 2010).

[34] M. S. Dresselhaus, G. Dresselhaus, and A. Jorio, *Group Theory: Application to the Physics of Condensed Matter* (Springer Science & Business Media, Berlin, 2007).

[35] D. S. Wang, R. Wu, and A. J. Freeman, First-principles theory of surface magnetocrystalline anisotropy and the diatomic-pair model, Phys. Rev. B **47**, 14932 (1993).

[36] D. Odkhuu, W. S. Yun, S. H. Rhim, and S. C. Hong, Theory of perpendicular magnetocrystalline anisotropy in Fe/MgO (001), J. Magn. Magn. Mater. **414**, 126 (2016).

[37] T. H. Ho, D. Odkhuu, S. H. Rhim, and S. C. Hong, First-principles study on magnetocrystalline anisotropy of cobalt films: Hcp vs fcc, Curr. Appl. Phys. **41**, 148 (2022).

[38] Q.-ul-ain, D. Odkhuu, S. H. Rhim, and S. C. Hong, Enhanced voltage-controlled magnetic anisotropy via magnetoelasticity in FePt/MgO(001), Phys. Rev. B **101**, 214436 (2020).

[39] P. Weiss, L'hypothèse du champ moléculaire et la propriété ferromagnétique, J. Phys. Theor. Appl. **6**, 661 (1907).

[40] R. Skomski, *Simple Models of Magnetism* (Oxford University Press, Oxford, 2008).

[41] J. S. Smart and J. H. Van Vleck, Effective field theories of magnetism, Phys. Today **19**(8), 77 (1966).

[42] C. Binek, *Ising-Type Antiferromagnets: Model Systems in Statistical Physics and in the Magnetism of Exchange Bias* (Springer Science & Business Media, Berlin, 2003).

[43] J. M. D. Coey, *Rare-Earth Iron Permanent Magnets* (Oxford University Press, Oxford, 1996).

[44] N. Goldenfeld, *Lectures on Phase Transitions and the Renormalization Group* (Addison-Wesley, Reading, 1992).

[45] B. Liu, Y. Zou, S. Zhou, L. Zhang, Z. Wang, H. Li, Z. Qu, and Y. Zhang, Critical behavior of the van der Waals bonded high T_C ferromagnet Fe_3GeTe_2, Sci. Rep. **7**, 6184 (2017).